\$ SUPER

Contents lists available at ScienceDirect

Scripta Materialia

journal homepage: www.journals.elsevier.com/scripta-materialia



Check for updates

Functionally graded stainless steels with tailored grain boundary serration

Y. Nie, Y.T. Chang, M.A. Charpagne

Department of Materials Science and Engineering, University of Illinois at Urbana-Champaign, IL, United States

ARTICLE INFO

Keywords: Grain boundaries Serration Functionally graded materials Stainless steel Additive manufacturing

ABSTRACT

We demonstrate the possibility of spatially controlling the degree of grain boundary serration in functionally graded stainless steels, by alloying powder mixtures on-the-fly during directed energy deposition additive manufacturing. Grain boundary serration is an attractive feature in polycrystalline microstructures, as it confers superior resistance to crack propagation and hot corrosion. Quantitative measurements at the microstructure scale coupled with thermodynamic calculations allow us to propose a mechanism to explain the origin of grain boundary serration. The formation of transient δ ferrite during solidification and its subsequent dissolution during cooling, governed by the Cr/Ni ratio, leads to the formation of remnant ferrite particles that hinder the growth of austenite grains in the solid state via a Smith-Zener pinning phenomenon. This finding opens new perspectives for grain boundary engineering, in-situ during additive manufacturing.

Functional grading is an exciting and nascent strategy in materials design that holds significant promises for achieving precise control over the mechanical [1,2], thermal [3], or environmental properties [4] locally. Additive manufacturing (AM), powder-fed directed energy deposition (DED) in particular, has quickly emerged as a powerful tool for fabricating functionally graded materials (FGMs) [5]. Highly versatile, DED uses separate powder feeders for each material, which enables multi-material deposition [6]. Functional grading using DED has been not only shown to achieve precise composition control [7-9], but it has also emerged as a powerful tool to design new alloys on-the-fly, by co-depositing multiple materials with varied ratio [10]. Beyond the intended chemical gradient, functional grading sometimes leads to intricate microstructures with drastic topological variations across the graded regions, including dense GB networks [11–13]. The GB network of polycrystalline materials controls most of their thermal, mechanical and environmental properties [14,15]. Decades of research efforts have been aimed at tailoring this network using approaches such as grain boundary engineering (GBE) [16-19]. One particularly sought topological feature GB serration (GBS): first evidenced by Koul et al. [20], GBS has been shown to improve creep resistance [21,22] by lowering the cavitation rate and slowing down crack propagation [23,24] up to 850 °C in superalloys. GBS also alleviates hot corrosion by hindering the percolation of sulfur and oxygen [25]. GBS is ubiquitous to many classes of materials including nickel superalloys [23,26-29], stainless steel [30-34], aluminum alloys [35], magnesium alloys [15,36] as well as high entropy alloys (HEAs) [37,38]. The mechanisms of GBS have been vastly investigated in wrought nickel superalloys, where it is conventionally triggered via solid state processing through dedicated annealing treatments. GBS arises from the discontinuous precipitation of second phase particles during cooling from supersolvus temperature [27,28,39], typically γ^{\prime} (Ni₃Al) [26,40], $\gamma^{\prime\prime}$ or δ (Ni₃Nb) [41] precipitates or M₂₃C₆, M₇C₃ carbides. The main mechanism leading to GBS is similar to Smith-Zener pinning: upon cooling, second-phase particles exert a counteracting pressure on migrating grain boundaries, locally inhibiting their motion. The part of the boundary that is in contact with the particle remains stationary while the rest of the boundary moves slightly, leading to a wavy topology. Fundamental knowledge of the mechanisms at the origin of GBS has been leveraged into new alloy design paradigms [20,42,43] as well as innovative processing pathways [44] for wrought polycrystalline alloys with superior performance.

Here, we reveal the presence of intense GBS variations as a function of the Cr/Ni ratio, in functionally graded stainless steel produced via insitu alloying using DED AM. Unlike previously documented GBS mechanisms, the serrations are formed dynamically during solidification, with δ ferrite particles serving as pinning sites to the growth of austenite grains. Concurrent thermodynamic calculations reveal a direct correlation between the degree of GBS and the transition in solidification mode: austenite-to-ferrite (AF) in alloys with low Cr/Ni ratio versus ferrite-to-austenite (FA) in alloys of high Cr/Ni ratio. Quantification of serration indices correlate with the pinning pressure by ferrite particles, and depends on the fraction of transient ferrite formed during solidification.

E-mail address: mcharp@illinois.edu (M.A. Charpagne).

 $^{^{\}ast}$ Corresponding author.

Gas atomized 304L and 316L powders with diameter in the 45 μm - $105\,\mu m$ range and respective composition (in wt.%) Fe-18.62%Cr-9.52% Ni-1.3%Mn-0.02%Cu-0.75%Si-0.018%C-0.02%O-0.01%P-0.004%S-0.07%N and Fe-17.6%Cr-12.6%Ni-0.89%Mn-2.43%Mo-0.67%Si-0.019%C-0.02%O-0.007%P-0.004%S-0.09%N, were purchased from Carpenter Technologies. N, O and C were measured by LECO analysis and other elements via Inductively Coupled Plasma Optical Emission spectroscopy. Parallelepiped-shaped specimens measuring 1.2 cm (w) x 2.5 cm (l) x 3 cm (h) were built onto a low carbon steel plate using a Formalloy L2 direct energy deposition (DED) system equipped with a 1 kW Nd:YAG laser (wavelength 1070 nm) and gaussian energy profile. Argon was used as shielding and carrier gas.

304L, 316L and graded specimens were printed using the same process parameters: a laser power of 500 W, a scan speed of 1100 mm/s and a scan rotation of 90° between adjacent layers. Built samples were removed from the base plate using a band saw and cut using a slowspeed saw. All samples were mechanically ground using SiC abrasive papers, followed by diamond alumina and colloidal silica suspensions down to 0.05 µm in diameter. X-ray diffractograms were acquired on all printed specimens using a PanAlytical X'Pert Pro-MPD with Cu Kα radiation ($\lambda = 0.154$ nm) under an acceleration voltage of 40 kV. Continuous θ -2 θ scans were collected with a step size of 0.01° and a collection time of 0.2 s/step. The microstructure of all specimens was characterized using a ThermoFischer Scientific (TFS) Scios2 scanning electron microscope (SEM) equipped with an Edax Hikari Super electron backscatter diffraction (EBSD) camera with a charged-coupled device (CCD) detector of 640×480 pixels and an EDAX Ametek Octane Elite Super energy dispersive spectroscopy (EDS) detector with a 70 mm² window. Back-scatter electrons (BSE) images, EDS and EBSD datasets were collected under an acceleration voltage of 30 kV over regions encompassing at least 4 melt pools and over 1000 individual grains, using a maximum step size of 1.5 µm. Twin-jet polishing was employed to prepare electron-transparent foils from 70 μm thick samples, using an HClO4 acid mix chilled to $-30\,^{\circ}\text{C}$. A TFS Talos transmission electron microscope (TEM) operated at 200 kV and equipped with a 4k x 4k Ceta™ 16 M camera and a super-X EDS system was used to characterize the thin foils. Thermodynamic calculations were performed using the ThermoCalc2022b software, TCFE 12, MOBFE7 database.

Fig. 1 shows EBSD maps of all printed materials. The build direction (BD) is normal to the surface, and maps are shown in inverse pole figure (IPF) colors indicating which crystallographic direction is parallel to the BD. High angle GBs, defined as those with a misorientation greater than 15°, are highlighted in black. While all materials exhibit a columnar grain structure (Fig. 1a,c), the GB morphology appears qualitatively planar in 316L (Fig. 1a) and strikingly wavy in the 304L material. The graded material is composed of 5 contiguous regions with 304L/316L ratios of 10/90, 30/70, 50/50, 70/30 and 90/10, deposited from bottom to top. Each region, highlighted in Fig. 1b, contains 10 deposition layers. Fig. 1b shows a polished cross-section of the functionally graded material, etched with Carpenter's reagent. No defects were observed in the FGM, printed with a single set of manufacturing parameters. Melt pools are contiguous from one layer to the other with no visible printing instabilities between the graded regions. Samples were cut from each graded region for more detailed characterization. Fig. 1c shows that GBS qualitatively increases with increasing 304L/316L ratio, without significant change in grain size (see suppl. mat. A for grain size measurements). A sharp transition in GB morphology is visible from regions with a 304L/316L ratio of 50/50 to 70/30. The Cr, Mo, Ni and Mn contents, measured by SEM-EDS, are shown in Fig. 2a. As intended, all elements vary linearly across the gradient, with increasing Cr and Mn and decreasing Ni and Mo with increasing 304L fraction.

To characterize GBS quantitatively, we use the serration index developed by Tang et al. [24]. This index depicts the area carved out relative to a smooth boundary by incorporating both the wavelength [23,45] and protrusion height of GBs, which makes it the most objective and reliable method to quantify GBS so far. The method consists in

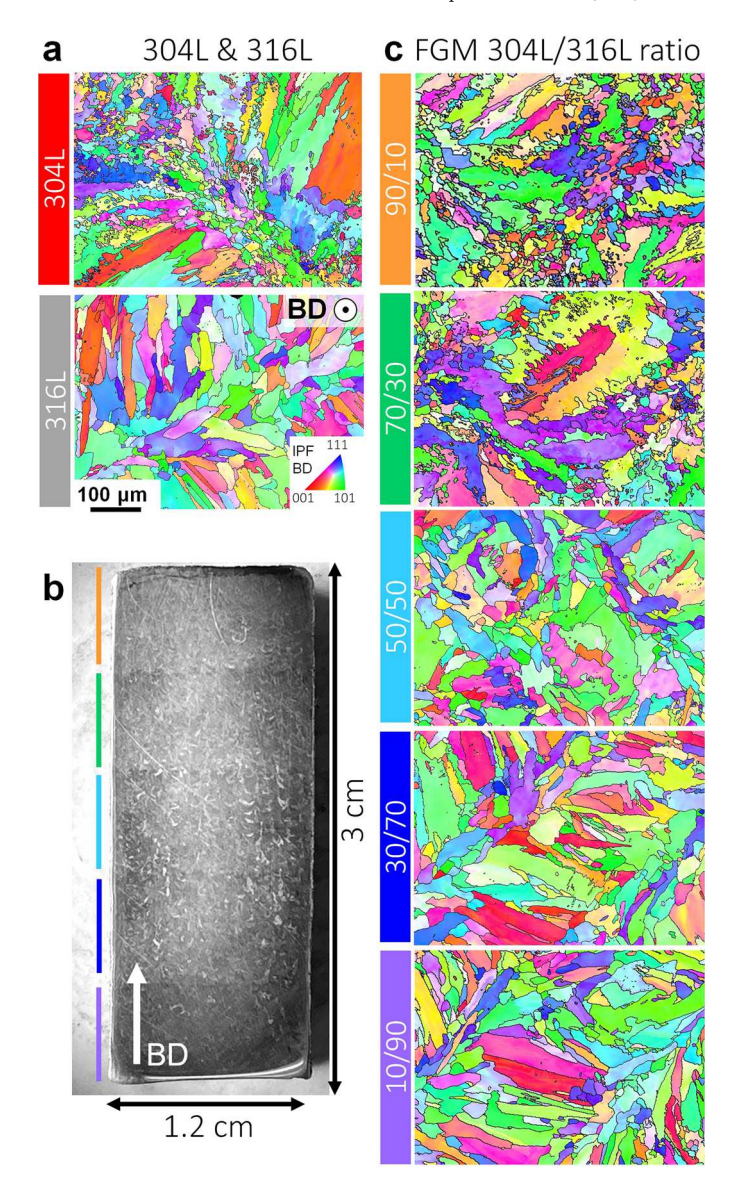


Fig. 1. Microstructure of all printed materials. a) EBSD maps of 304L and 316L, b) macro-etched functionally graded sample, c) EBSD maps of the five regions in the FGM. All EBSD maps are coded in IPF colors with respect to the build direction, normal to the surface.

measuring successive distances between a straight line drawn parallel to the boundary. A fast Fourier transformation is applied on the profile of distances, which reveals the individual wavelength and amplitude of each serration present in the boundary. The overall shape of the boundary is represented by its three waves with the highest amplitude [24]. The wavelength and amplitude of these three waves are multiplied which yields three indices per boundary. The overall serration index is defined as the average value of the three and has units of μm^2 . Here, at least 15 individual high angle boundaries were characterized per microstructure, chosen randomly.

Fig. 2b shows the serration indices with increasing fraction of 304L alloy from left to right. The markers correspond to the average serration index and the bars to the standard deviation. The mean serration index increases monotonously with the 304L fraction. 316L, 10/90 and 30/70 regions possess indices around 15 μm^2 . The 50/50 and 70/30 regions are characterized by a large span of GBS indices which is consistent with the mix of serrated and relatively smoother boundaries in Fig. 1c. Regions containing over 90% of 304L exhibit significantly higher GBS. All boundaries are serrated, as seen in Fig. 1a,c. It is worth noting that these

Scripta Materialia 237 (2023) 115714

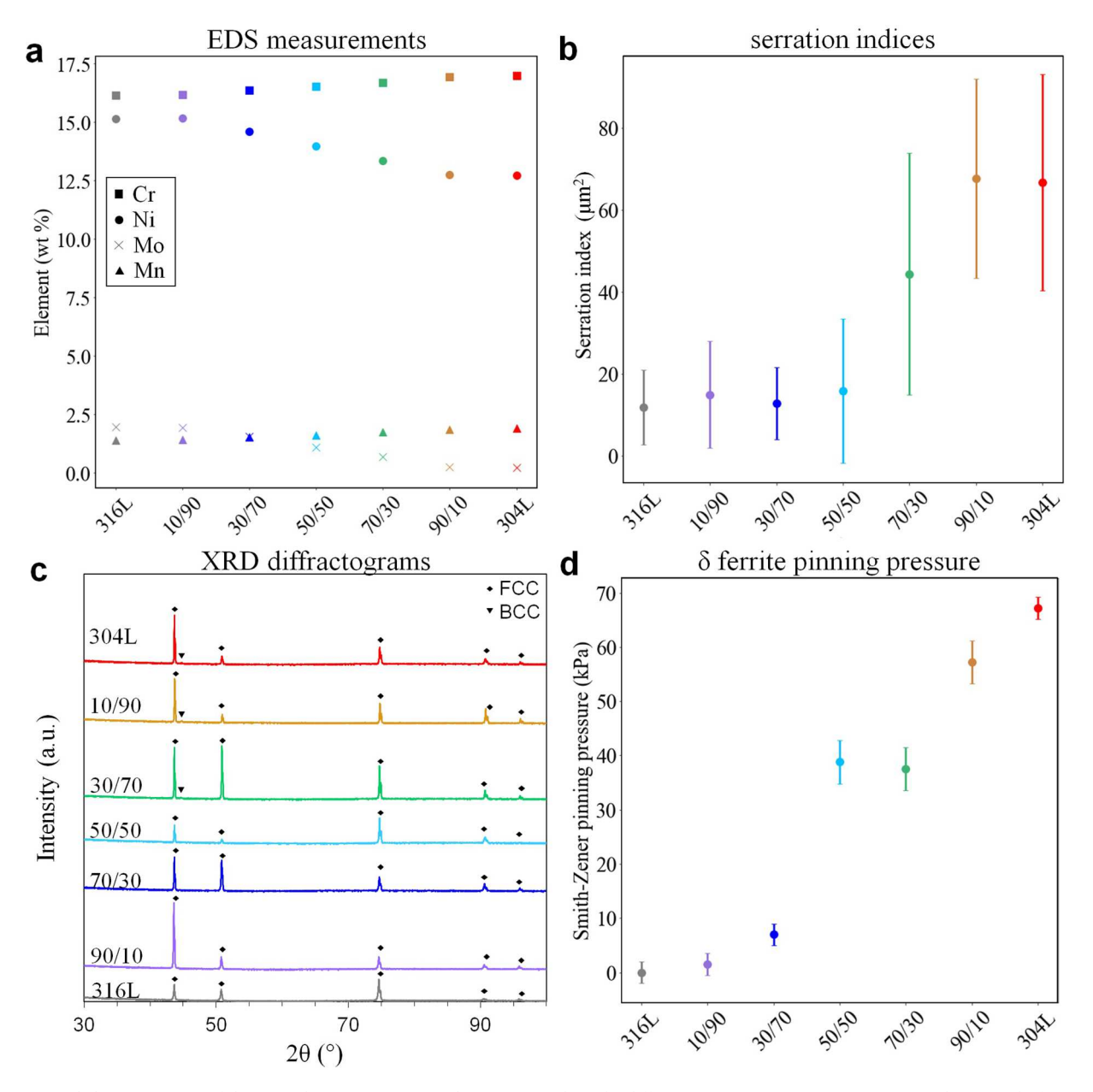


Fig. 2. Statistical characterization of the printed microstructures. Colors corresponds to the different regions in Fig. 1. a) Cr, Ni, Mo and Mn weight fractions from SEM-EDS maps, b) serration indices using the method from Tang et al. [24], c) X-ray diffractograms, d) Smith-Zener pinning pressure from δ ferrite. The fractions in the x-axis correspond to the 304L/316L ratios.

values are substantially higher than those reported in wrought microstructures after dedicated thermal GBS processing [24], which typically fall in the 10–25 μm^2 range. X-ray diffractograms shown in Fig. 2c, reveal that alloys containing over 90% 304L contain BCC δ ferrite, in addition to the FCC γ austenite.

Close inspection of the GB structure reveals a strikingly different morphology in 316L-rich (Fig. 3a,b,c) versus 304L-rich alloys (Fig. 3d,e,f). While all microstructures exhibit cellular structures, their segregation profiles are drastically different. In 316L-rich alloys, cell walls are enriched in Ni, Cr and Mo (Fig. 3b,c). In 304L-rich alloys Ni segregates to the core of the cells and Cr at the cell walls (Fig. 3f), where 50–100 nm thick δ ferrite particles are observed (Fig. 3d,e). Interestingly, GBs align with cell boundaries in 304L-rich alloys (Fig. 3d), where the GB is pinned by δ ferrite particles, while no such observation can be made in 316L-rich alloys (Fig. 3a). These observations suggest different solidification modes as a function of the alloy composition. The solidification mode in Fe-Cr-Ni-Mn steels is governed by the ratio between ferrite

versus austenite stabilizers, Cr_{eq}/Ni_{eq} . Utilizing the SEM-EDS measurements in Fig. 2a, we calculated the Cr_{eq}/Ni_{eq} ratio in our alloys, shown as vertical lines in Fig. 4b, and compared with the theoretical solidification mode predicted from the pseudo-binary phase diagram in Fig. 4a. These results suggest that alloys 316L, 10/90, 30/70 and 50/50 would solidify following an AF mode, while alloys 70/30, 90/10 and 304L solidify following a FA mode.

In AF mode, austenitic cells grow following the steepest thermal gradient, in colonies separated by GBs [46–48]. The partitioning coefficients of Cr, Mo and Ni in austenite (k ζ_{r} , k ζ_{Mo} and k ζ_{Ni}) are < 1, indicating that they are rejected into the liquid while austenite grows [49–52]. This solute partitioning creates the characteristic AF micro-segregation profile observed in Fig. 3c, with Cr, Mo, and Ni enrichment at cell boundaries. As the Creq/Nieq ratio increases at cell boundaries, ferrite can occasionally form via a eutectic reaction [50]. Dislocations accumulate on the cell boundaries as a result of thermal stress [53–55]. The main driving force for grain boundary migration is

Y. Nie et al. Scripta Materialia 237 (2023) 115714

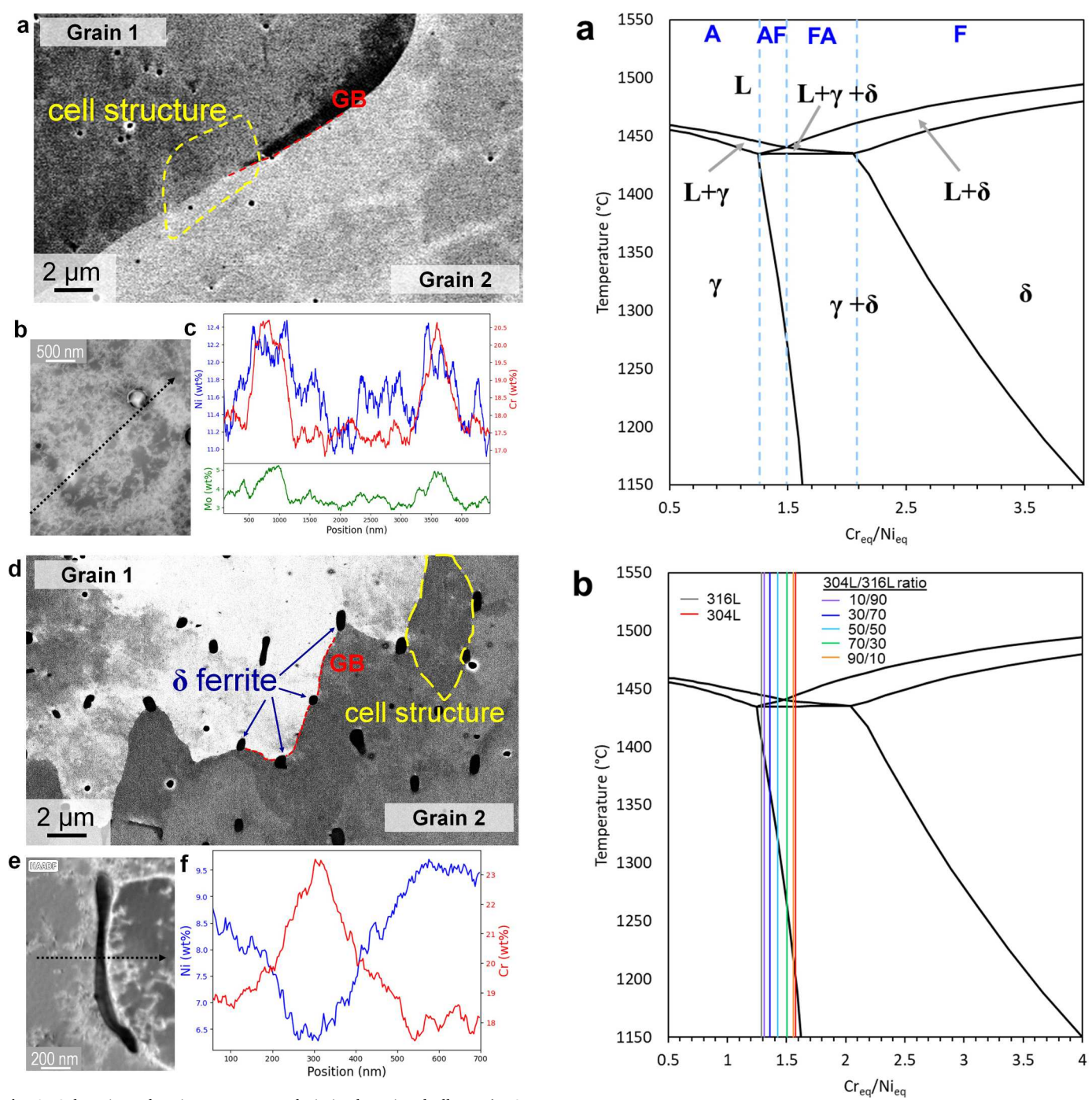


Fig. 3. Sub-grain scale microstructure analysis in the printed alloys. a) BSE image showing orientation and phase contrast in the 10/90 material, b) STEM-HAADF image in 316L and c) corresponding TEM-EDS composition profile showing enrichment of Ni, Cr and Mo at the cell walls (arrow in b), d) BSE image in 90/10 material showing a GB pinned by δ ferrite particles and cell structures spatially correlated with GBs, e) STEM-HAADF image in 304L and f) corresponding TEM-EDS composition profile showing enrichment of Cr and depletion of Ni at the cell walls (arrow in e).

the reduction in GB surface area [51], which leads to smooth GBs in 316L, 10/90, 30/70 and 50/50 alloys, that do not coincide with the microsegregation pattern (Fig. 3a).

In contrast, 70/30, 90/10 and 304L alloys solidify in FA mode (Fig. 4b) where the primary solidification front is ferritic and transforms to austenite via a solid-state transformation [50,51,56,57]. At the onset of solidification, Ni is rejected from the ferritic solidification front into the liquid, as $k_{\rm Ni}^{\delta} < 1$ [50]. The cell cores are enriched in Cr and possess a

Fig. 4. Pseudo-binary $FeNi_{eq}Cr_{eq}$ phase diagrams obtained from Thermocalc. a) phase map with solidification modes highlighted in blue dashed lines, b) composition of our printed alloys measured by EDS overlapped with the phase map. Colors correspond to the different regions in Fig. 1.

low Cr_{eq}/Ni_{eq} ratio at their boundaries, which promotes the nucleation of austenite in the intercellular regions. The ferrite-to-austenite transformation occurs through the migration of the γ - δ interface into the original ferrite, governed by short-range trans-interphase diffusion of Ni into austenite, while Cr and other ferrite stabilizers partition to ferrite [50]. This results in opposite Cr versus Ni microsegregation profiles as shown in Fig. 3f, characteristic of FA solidification [50,51,58], and retained ferrite enveloped by the new γ cell structure. A closer inspection of serrated GBs, in Fig. 5, reveals two driving forces acting concurrently onto them: strain-induced boundary migration (SIBM) and

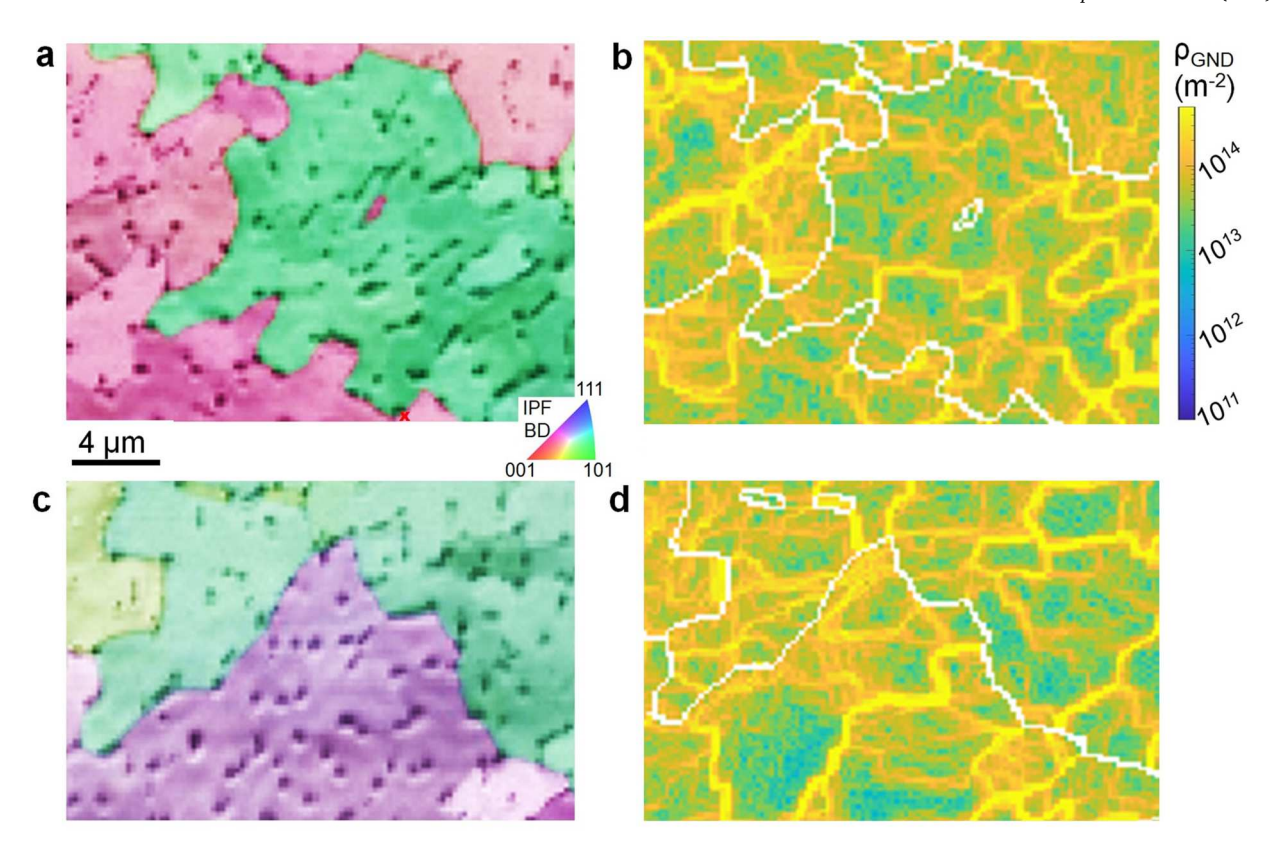


Fig. 5. EBSD maps around two serrated GBs in 304L. a) IPF-colored map overlapped by transparency with the index quality (IQ) map in greyscale, where δ particles appear as dark features; b) corresponding GND density map; c) IPF-IQ maps in a second region; d) corresponding GND density map with GBs in white.

Smith-Zener pinning. Fig. 5a,c show composite EBSD maps in IPF colors overlapped with the index quality (IQ) in greyscale, showing δ phase as darker particles. Numerous δ particles are visibly pinning the GBs, creating serrations. Fig. 5b,d show the corresponding EBSD maps colored according to the density of geometrically necessary dislocations (GNDs) [59]. The presence of remnant dislocation densities in the vicinity of serrated GBs is indicative of the presence of a driving force for SIBM [15,60,61]. These results suggest that GBS is the product of the balance between SIBM, driving force for boundary migration, and Smith-Zener pinning, a restraining force to GB motion.

GNDs could arise from multiple phenomena. Sheil calculations in DED 304L indicate that solidifying grains are subject to tensile stresses as the surrounding liquid contracts [62]. The high number of slip systems available in BCC δ ferrite, combined with its low yield strength at high temperature, can lead to plastically deformed ferritic grains, that accumulate misorientation as they solidify [63]. Geometrically necessary dislocations (GNDs) arise to maintain the continuity of the deformation field [64,65], leading to long-range 3D misorientation fields that could be inherited by the austenite grains, as observed in [62]. Furthermore, γ and δ phases possess different coefficients of thermal expansion which can also increase the dislocation density during the ferrite-to-austenite phase transformation [50,66].

Although determination of the exact mechanism would require insitu observation at the sub-cell scale during solidification, it is clear that GB pinning by δ ferrite plays a critical role in inducing GBS. To gain quantitative insight onto this effect, we calculate the Smith-Zener pinning pressure P_Z in all alloys, defined as:

$$P_Z = \frac{3\gamma_{GB}f}{d} \tag{1}$$

where γ_{GB} is the grain boundary energy (here 0.835 J/m² [67]), f and d are the fraction and average equivalent diameter of δ ferrite respectively, measured from back-scattered images (see suppl. mat. B for an

example). The calculated pinning pressures are shown in Fig. 2d. The small ferrite fraction measured in AF-solidifying alloys corresponds to eutectic ferrite (see suppl. mat. C). While GBS likely occurred at a temperature where the fraction and size of δ particles were different, comparison with Fig. 2b shows a clear correlation between the serration index and pinning force with increasing Cr_{eq}/Ni_{eq} ratio. In summary, we show that the solidification mode governs the grain structure development in AM stainless steels. Tailoring the Cr_{eq}/Ni_{eq} ratio allows to tune the fraction of transient ferrite formed during solidification, hence its Smith-Zener pinning pressure and the degree of GBS. Furthermore, we demonstrate the possibility of spatially controlling GBS via functional grading using a single set of printing parameters in DED. This mechanism can be leveraged into a new alloy design paradigm for in-situ GBE during AM.

We gratefully acknowledge support from the National Science Foundation, CAREER award DMR-2236640, as well as the Energy and Biosciences Institute (EBI-Shell program). We thank JC. Stinville (UIUC), K. Zhang and M. Reynolds (Shell) for insightful discussions. We acknowledge the use of facilities and instrumentation at the Materials Research Laboratory Central Research Facilities, University of Illinois, partially supported by NSF through the University of Illinois Materials Research Science and Engineering Center DMR-1720633.

Declaration of Competing Interest

The authors declare that they have no known competing financial interests or personal relationships that could have appeared to influence the work reported in this paper.

Supplementary materials

Supplementary material associated with this article can be found, in the online version, at doi:10.1016/j.scriptamat.2023.115714.

References

- [1] S.W. Yang, J. Yoon, H. Lee, D.S. Shim, Defect of functionally graded material of inconel 718 and sts 316l fabricated by directed energy deposition and its effect on mechanical properties, J. Mater. Res. Technol. 17 (2022) 478–497, https://doi. org/10.1016/j.jmrt.2022.01.029.
- [2] B.S. Shariat, Q. Meng, A.S. Mahmud, Z. Wu, R. Bakhtiari, J. Zhang, F. Motazedian, H. Yang, G. Rio, T. Hyun Nam, Y. Liu, Functionally graded shape memory alloys: design, fabrication and experimental evaluation, Mater. Des. 124 (2017) 225–237, https://doi.org/10.1016/j.matdes.2017.03.069.
- [3] B. Onuike, B. Heer, A. Bandyopadhyay, Additive manufacturing of inconel 718—Copper alloy bimetallic structure using laser engineered net shaping (lens™), Addit, Manuf. 21 (2018) 133–140, https://doi.org/10.1016/j.addma.2018.02.007.
- [4] L. Thivillon, P. Bertrand, B. Laget, I. Smurov, Potential of direct metal deposition technology for manufacturing thick functionally graded coatings and parts for reactors components, J. Nucl. Mater. 385 (2009) 236–241, https://doi.org/ 10.1016/j.jnucmat.2008.11.023, nuclear Materials III.
- [5] M. Naebe, K. Shirvanimoghaddam, Functionally graded materials: a review of fabrication and properties, Appl. Mater. Today 5 (2016) 223–245, https://doi.org/ 10.1016/j.apmt.2016.10.001
- [6] D. Dev Singh, S. Arjula, A. Raji Reddy, Functionally graded materials manufactured by direct energy deposition: a review, Materials Today: proceedings, in: international Conference on Materials and System Engineering 47, 2021, pp. 2450–2456, https://doi.org/10.1016/j.matpr.2021.04.536.
- [7] M. Ansari, E. Jabari, E. Toyserkani, Opportunities and challenges in additive manufacturing of functionally graded metallic materials via powder-fed laser directed energy deposition: a review, J. Mater. Process. Technol. 294 (2021), 117117, https://doi.org/10.1016/j.jmatprotec.2021.117117.
- [8] L.D. Bobbio, B. Bocklund, E. Simsek, R.T. Ott, M.J. Kramer, Z.K. Liu, A.M. Beese, Design of an additively manufactured functionally graded material of 316 stainless steel and ti-6al-4v with ni-20cr, cr, and v intermediate compositions, Addit. Manuf. 51 (2022), 102649, https://doi.org/10.1016/j.addma.2022.102649.
- [9] X. Zhang, L. Li, F. Liou, Additive manufacturing of stainless steel copper functionally graded materials via inconel 718 interlayer, J. Mater. Res. Technol. 15 (2021) 2045–2058, https://doi.org/10.1016/j.jmrt.2021.09.027.
- [10] N. Sargent, Y. Wang, D. Li, Y. Zhao, X. Wang, W. Xiong, Exploring alloy design pathway through directed energy deposition of powder mixtures: a study of stainless steel 3161 and inconel 718, Addit. Manuf. Lett. 6 (2023), 100133, https:// doi.org/10.1016/i.addlet.2023.100133.
- [11] M. Gushchina, O. Klimova-Korsmik, G. Turichin, Direct laser deposition of cu-mo functionally graded layers for dissimilar joining titanium alloys and steels, Mater. Lett. 307 (2022), 131042, https://doi.org/10.1016/j.matlet.2021.131042.
- [12] S. Mao, D.Z. Zhang, Z. Ren, G. Fu, X. Ma, Effects of process parameters on interfacial characterization and mechanical properties of 316l/cucrzr functionally graded material by selective laser melting, J. Alloys Compd. 899 (2022), 163256, https://doi.org/10.1016/j.jallcom.2021.163256.
- [13] Z. Hu, Z. Ma, L. Yu, Y. Liu, Functionally graded materials with grain-size gradients and heterogeneous microstructures achieved by additive manufacturing, Scr. Mater. 226 (2023), 115197, https://doi.org/10.1016/j.scriptamat.2022.115197.
- [14] Z.C. Cordero, B.E. Knight, C.A. Schuh, Six decades of the hall–petch effect a survey of grain-size strengthening studies on pure metals, Int. Mater. Rev. 61 (2016) 495–512, https://doi.org/10.1080/09506608.2016.1191808.
- [15] H.W. Son, J.W. Lee, S.K. Hyun, Mechanism of grain boundary serration during hot deformation of az31 alloy: role of grain boundary dislocations and grain boundary sliding, Int. J. Plast. 125 (2020) 118–132, https://doi.org/10.1016/j. iinlas 2019 09 003
- [16] C.A. Schuh, M. Kumar, W.E. King, Analysis of grain boundary networks and their evolution during grain boundary engineering, Acta Mater. 51 (2003) 687–700, https://doi.org/10.1016/S1359-6454(02)00447-0.
- [18] T. Watanabe, Grain boundary engineering: historical perspective and future prospects, J. Mater. Sci. 46 (2011) 4095–4115, https://doi.org/10.1007/s10853-011 5003 g
- [19] M. Seita, S. Gao, Broadening the design space of engineering materials through "additive grain boundary engineering, J. Mater. Sci. 57 (2022) 9530–9540, https://doi.org/10.1007/s10853-022-06886-6.
- [21] A. Wisniewski, J. Beddoes, Influence of grain-boundary morphology on creep of a wrought ni-base superalloy, Materials Science and Engineering: a 510-511 (2009), in: 11th International Conference of Creep and Fracture of Engineering Materials and Structures, CREEP, 2008, pp. 266–272, https://doi.org/10.1016/j. msea 2008.04.130
- [22] A.C. Yeh, K.W. Lu, C.M. Kuo, H.Y. Bor, C.N. Wei, Effect of serrated grain boundaries on the creep property of inconel 718 superalloy, Mater. Sci. Eng. A Struct. Mater. 530 (2011) 525–529, https://doi.org/10.1016/j.msea.2011.10.014.
- [23] H. Hong, I. Kim, B. Choi, M. Kim, C. Jo, The effect of grain boundary serration on creep resistance in a wrought nickel-based superalloy, Mater. Sci. Eng. A Struct. Mater. 517 (2009) 125–131, https://doi.org/10.1016/j.msea.2009.03.071.
- [24] Y.T. Tang, A.J. Wilkinson, R.C. Reed, Grain boundary serration in nickel-based superalloy inconel 600: generation and effects on mechanical behavior, Metall. Mater. Trans. A 49 (2018) 4324–4342, https://doi.org/10.1007/s11661-018-4671-7.

- [25] P. Bhuyan, S. Pradhan, R. Mitra, S. Mandal, Evaluating the efficiency of grain boundary serrations in attenuating high-temperature hot corrosion degradation in alloy 617, Corros. Sci. 149 (2019) 164–177, https://doi.org/10.1016/j. corsci.2019.01.007.
- [26] H.L. Danflou, M. Marty, A. Walder, Formation of serrated grain boundaries and their effect on the mechanical properties in a p/m nickel base superalloy, in: Superalloys 1992 Conference Proceedings, 1992.
- [27] L. Jiang, R. Hu, H. Kou, J. Li, G. Bai, H. Fu, The effect of m23c6 carbides on the formation of grain boundary serrations in a wrought ni-based superalloy, Mater. Sci. Eng. A Struct. Mater. 536 (2012) 37–44, https://doi.org/10.1016/j.msea.2011.11.060.
- [28] Y.S. Lim, D.J. Kim, S.S. Hwang, H.P. Kim, S.W. Kim, M23c6 precipitation behavior and grain boundary serration in Ni-based alloy 690, Mater. Charact. 96 (2014) 28–39, https://doi.org/10.1016/j.matchar.2014.07.008.
- [29] B. Alabbad, L. Li, S. Tin, Controlling the grain boundary morphology and secondary γ' precipitate size distribution in ni-base superalloys, J. Alloys Compd. 775 (2019) 931–941, https://doi.org/10.1016/j.jallcom.2018.10.031.
- [30] O. Miyagawa, M. Yamamoto, M. Kobayashi, Zig-zag grain boundaries and strength of heat resisting alloys, in: Superalloys 1976 conference proceedings, 1976, np. 245–254
- [31] H. Hong, S. Nam, The occurrence of grain boundary serration and its effect on the m23c6 carbide characteristics in an aisi 316 stainless steel, Mater. Sci. Eng. A Struct. Mater. 332 (2002) 255–261, https://doi.org/10.1016/S0921-5093(01) 01754-3
- [32] K. Kim, H. Hong, S. Nam, A study on the mechanism of serrated grain boundary formation in an austenitic stainless steel, Mater. Chem. Phys. 126 (2011) 480–483, https://doi.org/10.1016/j.matchemphys.2010.12.025.
- [33] K. Kim, H. Hong, S. Nam, Investigation on the formation of serrated grain boundaries with grain boundary characteristics in an aisi 316 stainless steel, J. Nucl. Mater. 393 (2009) 249–253, https://doi.org/10.1016/j. jnucmat.2009.06.011.
- [34] H.U. Hong, S.W. Nam, Improvement of creep-fatigue life by the modification of carbide characteristics through grain boundary serration in an aisi 304 stainless steel, J. Mater. Sci. 38 (2003) 1535–1542, https://doi.org/10.1023/a: 1022989002179.
- [35] E. Konopleva, H. McQueen, E. Evangelista, Serrated grain boundaries in hot-worked aluminum alloys at high strains, Mater. Charact. 34 (1995) 251–264, https://doi.org/10.1016/1044-5803(95)00062-3.
- [36] H.W. Son, S.K. Hyun, Periodic formations of deformation twins and dislocation arrays via grain boundary sliding at serrated grain boundary in cold-shear-strained az31 alloy, Int. J. Plast. 135 (2020), 102815, https://doi.org/10.1016/j. iiplas.2020.102815.
- [37] S. Wu, T. Yang, B. Cao, J. Luan, Y. Jia, L. Xu, Y. Mu, T. Zhang, H. Kong, X. Tong, J. Peng, G. Wang, Q. Zhai, J. Lu, C. Liu, Multicomponent ni-rich high-entropy alloy toughened with irregular-shaped precipitates and serrated grain boundaries, Scr. Mater. 204 (2021), 114066, https://doi.org/10.1016/j.scriptamat.2021.114066.
- [38] J.L. Lee, P.T. Wang, K.C. Lo, P.K. Shen, N.T. Tsou, K. Kakehi, H. Murakami, C. W. Tsai, S. Gorsse, A.C. Yeh, Effect of serrated grain boundary on tensile and creep properties of a precipitation strengthened high entropy alloy, Sci. Technol. Adv. Mater. 24 (2023), https://doi.org/10.1080/14686996.2022.2158043.
- [39] Y.T. Tang, P. Karamched, J. Liu, J.C. Haley, R.C. Reed, A.J. Wilkinson, Grain boundary serration in nickel alloy inconel 600: quantification and mechanisms, Acta Mater. 181 (2019) 352–366, https://doi.org/10.1016/j.actamat.2019.09.037.
 [40] C. Qiu, P. Andrews, On the formation of irregular-shaped gamma prime and
- [40] C. Qiu, F. Andrews, On the formation of irregular-shaped gaining printe and serrated grain boundaries in a nickel-based superalloy during continuous cooling, Mater. Charact. 76 (2013) 28–34, https://doi.org/10.1016/j. matchar.2012.11.012.
- [41] E. Pickering, H. Mathur, A. Bhowmik, O. Messe, J. Barnard, M. Hardy, R. Krakow, K. Loehnert, H. Stone, C. Rae, Grain-boundary 'precipitation in allvac 718plus, Acta Mater. 60 (2012) 2757–2769, https://doi.org/10.1016/j. actamat.2012.01.042.
- [42] P. Bhuyan, S. Sanyal, V.S. Sarma, B. de Boer, R. Mitra, S. Mandal, A novel approach combining grain boundary engineering and grain boundary serration to enhance high-temperature hot corrosion resistance in alloy 617, Materialia 23 (2022), 101451, https://doi.org/10.1016/j.mtla.2022.101451.
- [43] K. Kim, J. Ginsztler, S. Nam, The role of carbon on the occurrence of grain boundary serration in an aisi 316 stainless steel during aging heat treatment, Mater. Lett. 59 (2005) 1439–1443, https://doi.org/10.1016/j.matlet.2004.12.050.
- [44] Y. Wu, H. Zhao, J. Li, Y. Zhang, J. Liu, T. Liu, An innovative approach towards forming the serrated grain boundaries and refining the γ' precipitates in nickelbased superalloys, J. Alloys Compd. 908 (2022), 164570, https://doi.org/10.1016/ i.iall.com.2022.164570.
- [45] R. Mitchell, H. Li, Z. Huang, On the formation of serrated grain boundaries and fan type structures in an advanced polycrystalline nickel-base superalloy, J. Mater. Process. Technol. 209 (2009) 1011–1017, https://doi.org/10.1016/j. imatprotec.2008.03.008.
- [46] O. Zinovieva, A. Zinoviev, V. Ploshikhin, Three-dimensional modeling of the microstructure evolution during metal additive manufacturing, Comput. Mater. Sci. 141 (2018) 207–220, https://doi.org/10.1016/j.commatsci.2017.09.018.
- [47] J. Song, Y. Chew, G. Bi, X. Yao, B. Zhang, J. Bai, S.K. Moon, Numerical and experimental study of laser aided additive manufacturing for melt-pool profile and grain orientation analysis, Mater. Des. 137 (2018) 286–297, https://doi.org/ 10.1016/j.matdes.2017.10.033.
- [48] A. Prasad, L. Yuan, P. Lee, M. Patel, D. Qiu, M. Easton, D. StJohn, Towards understanding grain nucleation under additive manufacturing solidification

- conditions, Acta Mater. 195 (2020) 392–403, https://doi.org/10.1016/j.actamat.2020.05.012.
- [49] P.L. Ferrandini, C.T. Rios, A.T. Dutra, M.A. Jaime, P.R. Mei, R. Caram, Solute segregation and microstructure of directionally solidified austenitic stainless steel, Mater. Sci. Eng. A 435-436 (2006) 139–144, https://doi.org/10.1016/j. msea.2006.07.024.
- [50] J.A. Brooks, A.W. Thompson, Microstructural development and solidification cracking susceptibility of austenitic stainless steel welds, Int. Mater. Rev. 36 (1991) 16–44, https://doi.org/10.1179/imr.1991.36.1.16.
- [51] T.R. Smith, J.D. Sugar, C.S. Marchi, J.M. Schoenung, Microstructural development in DED stainless steels: applying welding models to elucidate the impact of processing and alloy composition, J. Mater. Sci. 56 (2020) 762–780, https://doi. org/10.1007/s10853-020-05232-y.
- [52] Y. Arata, F. Matsuda, S. Katayama, Solidification crack susceptibility in weld metals of fully austenitic stainless steels, Trans. JWRI (Jpn. Weld. Res. Inst.) 5 (1976) 135–151.
- [53] K.M. Bertsch, G.M. de Bellefon, B. Kuehl, D.J. Thoma, Origin of dislocation structures in an additively manufactured austenitic stainless steel 316l, Acta Mater. 199 (2020) 19–33, https://doi.org/10.1016/j.actamat.2020.07.063.
- [54] Z. Liu, D. Zhao, P. Wang, M. Yan, C. Yang, Z. Chen, J. Lu, Z. Lu, Additive manufacturing of metals: microstructure evolution and multistage control, J. Mater. Sci. Technol. 100 (2022) 224–236, https://doi.org/10.1016/j. imst.2021.06.011.
- [55] D. Kong, C. Dong, S. Wei, X. Ni, L. Zhang, R. Li, L. Wang, C. Man, X. Li, About metastable cellular structure in additively manufactured austenitic stainless steels, Addit. Manuf. 38 (2021), https://doi.org/10.1016/j.addma.2020.101804.
- [56] Y. Fu, N. Guo, C. Zhou, G. Wang, J. Feng, Investigation on in-situ laser cladding coating of the 304 stainless steel in water environment, J. Mater. Process. Technol. 289 (2021), https://doi.org/10.1016/j.jmatprotec.2020.116949.
- [57] T. Zargar, F. Sadeghi, J.W. Kim, J.S. Lee, Y.U. Heo, C.H. Yim, Kinetic model to investigate the effect of cooling rate on δ-ferrite behavior and its application in continuous casting of aisi 304 stainless steel, Met. Mater. Int. 28 (2022) 2263–2276, https://doi.org/10.1007/s12540-021-01118-z.

- [58] J.A. Brooks, J.C. Williams, A.W. Thompson, Stem analysis of primary austenite solidified stainless steel welds, Metall. Mater. Trans. A (1983) 23–31, https://doi. org/10.1007/BF02643733.
- [59] MTEX, Geometrically Necessary Dislocations in Mtex, 2008. https://mtex-toolbox.github.io/GND.html.
- [60] A. Paggi, G. Angella, R. Donnini, Strain induced grain boundary migration effects on grain growth of an austenitic stainless steel during static and metadynamic recrystallization, Mater. Charact. 107 (2015) 174–181, https://doi.org/10.1016/j. matchar.2015.07.003.
- [61] K. Kashihara, H. Konishi, T. Shibayanagi, Strain-induced grain boundary migration in {112} {111}/{100} {001} and {123} {634}/{100} {001} aluminum bicrystals, Mater. Sci. Eng. A 528 (2011) 8443–8450, https://doi.org/10.1016/j. msea 2011 08 020
- [62] A.T. Polonsky, W.C. Lenthe, M.P. Echlin, V. Livescu, G.T. Gray, T.M. Pollock, Solidification-driven orientation gradients in additively manufactured stainless steel, Acta Mater. 183 (2020) 249–260, https://doi.org/10.1016/j. actamat.2019.10.047.
- [63] L. Gardner, A. Insausti, K. Ng, M. Ashraf, Elevated temperature material properties of stainless steel alloys, J. Constr. Steel Res. 66 (2010) 634–647, https://doi.org/ 10.1016/j.jcsr.2009.12.016.
- [64] H. Gao, Y. Huang, Geometrically necessary dislocation and size-dependent plasticity, Scr. Mater. 48 (2003) 113–118, https://doi.org/10.1016/s1359-6462 0200329.9
- [65] R.Z. Wang, L.Y. Cheng, S.P. Zhu, P.C. Zhao, H. Miura, X.C. Zhang, S.T. Tu, Semi-quantitative creep-fatigue damage analysis based on diffraction-based misorientation mapping and the correlation to macroscopic damage evolutions, Int. J. Fatigue 149 (2021), 106227, https://doi.org/10.1016/j.iifatigue.2021.106227.
- [66] I. Manna, Grain boundary migration in solid state discontinuous reactions, Interface Sci. 6 (1998) 113–131, https://doi.org/10.1023/a:1008672705642.
- [67] E.A. Trillo, A TEM investigation of m23c6 carbide precipitation behaviour on varying grain boundary misorientations in 304 stainless steels, J. Mater. Sci. 33 (1998) 1263–1271, https://doi.org/10.1023/a:1004390029071.